Univerzita Karlova v Praze
Matematicko-fyzikální fakulta

BAKALÁŘSKÁ PRÁCE

Katarína Tóthová

Numerické metody zpracování obrazu

Katedra numerické matematiky

Vedoucí bakalářské práce: RNDr. Iveta Hnětynková, Ph.D.
Studijní program: Numerická a výpočtová matematika

2010

I would like to express my sincere gratitude to my supervisor, RNDr. Iveta Hnětynková, Ph.D., for her academic guidance, patience and inspirational suggestions. Also, I wish to acknowledge my brother, who has kindly allowed me to use his photographic material for my experiments.

I hereby declare that I have completed my bachelor's thesis myself and that I have only used information from the referenced sources. I agree with further lending of the thesis and its public use for study purposes.

25th July 2010, Prague Katarína Tóthová

Contents

Introduction **5**

1 Image Deblurring Problems **7**
- 1.1 Introduction to the Problem 7
  - 1.1.1 Digital Image Representation 7
  - 1.1.2 Linear Deblurring Model 8
- 1.2 Characteristics of the Blurring Operator 11
  - 1.2.1 Blurring as a Two Dimensional Convolution Problem 12
  - 1.2.2 Singular Value Decomposition 13
  - 1.2.3 Ill-posed problems 16

2 Numerical Treatment of Image Deblurring Problems **18**
- 2.1 Image Deblurring Methods 18
  - 2.1.1 Direct Regularization Methods 19
  - 2.1.2 Iterative Regularization Methods 21
- 2.2 Stopping Criteria 23
  - 2.2.1 L-curve 26
  - 2.2.2 Generalized Cross Validation 27
  - 2.2.3 Discrepancy principle 28

3 Numerical Experiments **29**
  - Problem 1 29
  - Problem 2 31
  - Problem 3 34
  - Problem 4 37
  - Problem 5 38
  - Problem 6 40

Conclusion **42**

Bibliography **43**

Název práce: Numerické metody zpracování obrazu
Autor: Katarína Tóthová
Katedra (ústav): Katedra numerické matematiky
Vedoucí bakalářské práce: RNDr. Iveta Hnětynková, Ph.D.
e-mail vedoucího: hnetynkova@cs.cas.cz

Abstrakt: Cieľom tejto práce je podať ucelený prehľad vybraných numerických metód spracovania obrazu, konkrétne popísať konštrukciu, vlastnonsti a spôsoby riešenia problémov zaostrovania obrazu popísaných pomocou sústavy $Ax = b$. Tieto úlohy častokrát spadajú do skupiny tzv. ill-posed problémov so zle podmienenou maticou A, čím si vyžadujú špeciálny prístup. V tejto práci ponúkame stručný prehľad vybraných regularizačných techník, ktoré môžu byť v tomto prípade použité – či už ide o metódy priame (TSVD, Tikhonova regularizácia) alebo iteračné (CGLS, LSQR), spolu s príslušnými metódami pre voľbu regularizačného parametra – L-krivkou, GCV a princípom diskrepancie. Výklad je doplnený o numerické experimenty pracujúce s reálnymi obrazovými dátami.

Klíčová slova: zaostrovanie obrazu, ill-posed úlohy, regularizácia, zastavovacie kritériá

Title: Numerical techniques in image processing
Author: Katarína Tóthová
Department: Department of Numerical Mathematics
Supervisor: RNDr. Iveta Hnětynková, Ph.D.
Supervisor's e-mail address: hnetynkova@cs.cas.cz

Abstract: The aim of this thesis is to provide a concise overview of the numerical techniques in digital image processing, specifically to discuss the construction, properties and methods of solving of the image deblurring problems modelled by a linear system $Ax = b$. Often, these problems fall within a group of the ill-posed problems with severely ill-conditioned matrix A and hence require special numerical treatment. We provide a brief overview of selected regularization methods that can be used in this situation, including direct (TSVD, Tikhonov regularization) and iterative ones (CGLS, LSQR), together with the pertinent parameter-choice methods – L-curve, GCV and the discrepancy principle. The theoretical discussion is supplemented by the numerical experiments with real-life image data.

Keywords: image deblurring, ill-posed problems, regularization, parameter-choice methods

Introduction

You cannot depend on your eyes when your imagination is out of focus.
Mark Twain

With the advent of the digital era, many of the modern as well as classical scientific disciplines, such as astronomy, radiology or archaeology, have come to depend greatly on the use of digital imaging devices. Since recording of the input image data by telescope, magnetic resonance, etc., may lead to unwanted changes in the image information, including blurring and pollution by noise, this progress has stimulated the development of digital image restoration techniques. In this thesis, we shall concentrate on the image deblurring methods proposed by the numerical linear algebra.

Here, the process of deblurring digital images is based on the numerical treatment of the linear system $Ax = b$, with A standing for the blurring operator representing an imaging device acting on the exact image data x and yielding a blurred image b. Often, this problem belongs to the class of the so-called *ill-posed problems* [12], where the severe ill-conditioning of the blurring operator prevents the use of direct solution methods, e.g. Gaussian elimination. Hence the *regularization methods* are introduced [4], [12], [14]. These attempt to rid the solution of noise and obtain a desired sharp image. In order to do so, the regularization methods can either directly filter the singular value decomposition components of the blurring operator (e.g. TSVD, Tikhonov regularization; [4], [12], [14]) or work iteratively by projecting the large problem onto a Krylov subspace of the smaller dimensions (e.g. CGLS, LSQR; [4], [6], [16], [22], [23]). The use of the regularization methods requires a choice of a suitable value of the regularization parameter that would lead to a desirable approximation of the exact solution (sharp image). The popular *parameter-choice methods* include the L-curve [2], [11], [12], [15], GCV [7], [28] and the discrepancy principle [12], [18], etc.

This thesis provides a brief overview of the above-mentioned regularization and paremeter-choice methods. The discussion shall be accompanied by references for further reading, and numerical experiments.

We shall begin our discussion by presenting the fundamentals of the image deblurring problems in Chapter 1. This involves gray-scale and colour digital image representation, formulation of the mathematical model simulating the image recording and the construction of the blurring operator. The ill-posed nature of the deblurring problems shall be revealed by examining the singular value decomposition of the blurring operator.

In Chapter 2, we summarize the numerical techniques aimed at deblurring digital images. We shall present representatives of two classes of the regularization methods – direct (TSVD, Tikhonov regularization) and iterative ones (CGLS, LSQR). Consequently, the pertinent stopping criteria (parameter-choice methods) will be outlined – this includes the L-curve, GCV and the discrepancy principle.

Chapter 3 provides the numerical experiments, carried out in MATLAB, trying to illustrate the application of the techniques in question to the real-life image data.

Chapter 1

Image Deblurring Problems

1.1 Introduction to the Problem

1.1.1 Digital Image Representation

Digital image, as a discrete record of a continuous reality, consists of picture elements (pixels) capturing small rectangular areas of a recorded scene. In gray-scale images, each pixel carries information about the light intensity denoted by a value from range 0 (black) to 255 (white). In order to be able to process these digital images by means of mathematical techniques, we need a way to represent them as arrays of numbers.

$$\begin{bmatrix} 43 & 44 & 45 & 46 & 47 & 48 & 49 & 50 \\ 42 & 21 & 22 & 23 & 24 & 25 & 26 & 51 \\ 41 & 20 & 7 & 8 & 9 & 10 & 27 & 52 \\ 40 & 19 & 6 & 1 & 2 & 11 & 28 & 53 \\ 39 & 18 & 5 & 4 & 3 & 12 & 29 & 54 \\ 38 & 17 & 16 & 15 & 14 & 13 & 30 & 55 \\ 37 & 36 & 35 & 34 & 33 & 32 & 31 & 56 \\ 64 & 63 & 62 & 61 & 60 & 59 & 58 & 57 \end{bmatrix}$$

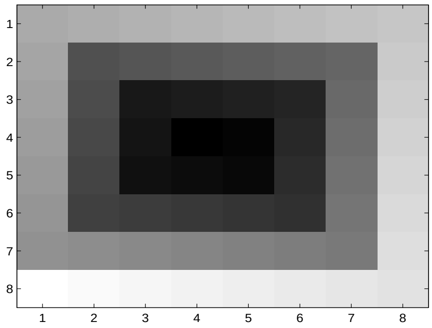

Figure 1.1 *Matrix representation of a gray-scale image.*

To begin with, consider first a black and white image of the size 8×8 pixels. Figure 1.1 shows the correspondence between the image and its underlying mathematical structure, a real 8×8 matrix. Note that the matrix was displayed using MATLAB *imagesc* function; this means the matrix elements were scaled onto $[0, 1]$ before being depicted as the light intensity levels.

Similarly, a colour image is handled as a 3-dimensional matrix of the size $n \times m \times 3$ with each 2-dimensional $n \times m$ array storing intensity information about one of the three *colour channels* (usually red, green and blue).

$$\begin{bmatrix} 0 & 0 & 0 & 0 & 0 & 0 & 0 & 0 \\ 0 & 0 & 0 & 0 & 0 & 0 & 0 & 0 \\ 0 & 1 & 1 & 1 & 1 & 0 & 0 & 0 \\ 0 & 1 & 1 & 1 & 1 & 0 & 0 & 0 \\ 0 & 1 & 1 & 1 & 1 & 0 & 0 & 0 \\ 0 & 1 & 1 & 1 & 1 & 0 & 0 & 0 \\ 0 & 0 & 0 & 0 & 0 & 0 & 0 & 0 \\ 0 & 0 & 0 & 0 & 0 & 0 & 0 & 0 \end{bmatrix}$$

Red

$$\begin{bmatrix} 0 & 0 & 0 & 0 & 0 & 0 & 0 & 0 \\ 0 & 0 & 0 & 0 & 0 & 0 & 0 & 0 \\ 0 & 0 & 0 & 1 & 1 & 0 & 0 & 0 \\ 0 & 0 & 0 & 1 & 1 & 0 & 0 & 0 \\ 0 & 0 & 0 & 1 & 1 & 0 & 0 & 0 \\ 0 & 0 & 0 & 1 & 1 & 0 & 0 & 0 \\ 0 & 0 & 0 & 0 & 0 & 0 & 0 & 0 \\ 0 & 0 & 0 & 0 & 0 & 0 & 0 & 0 \end{bmatrix}$$

Green

$$\begin{bmatrix} 0 & 0 & 0 & 0 & 0 & 0 & 0 & 0 \\ 0 & 0 & 0 & 0 & 0 & 0 & 0 & 0 \\ 0 & 0 & 0 & 0 & 0 & 1 & 1 & 0 \\ 0 & 0 & 0 & 0 & 0 & 1 & 1 & 0 \\ 0 & 0 & 0 & 0 & 0 & 1 & 1 & 0 \\ 0 & 0 & 0 & 0 & 0 & 1 & 1 & 0 \\ 0 & 0 & 0 & 0 & 0 & 0 & 0 & 0 \\ 0 & 0 & 0 & 0 & 0 & 0 & 0 & 0 \end{bmatrix}$$

Blue

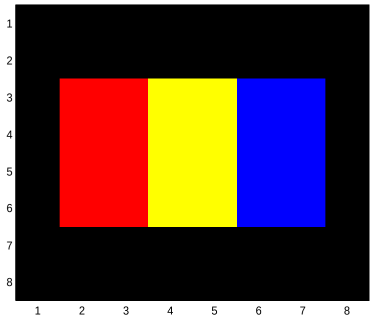

Figure 1.2 *3-D matrix representation of a colour image.*

1.1.2 Linear Deblurring Model

Gray-scale Images

Translating the digital image construction into mathematical language, we shall use a slightly different representation than the one described in the previous section – namely, digital images will be dealt with as *vectors* rather than matrices. Consider a gray-scale image of the size $n \times m$ pixels. The image vector $x \in \mathbb{R}^{nm}$ will be created by rearrangement of column elements $x_i \in \mathbb{R}^n$ of the coincident matrix $X \in \mathbb{R}^{n \times m}$, in such a way that $x = (x_1^T, x_2^T, ..., x_m^T)^T \in \mathbb{R}^{nm}$. Given a sharp real image

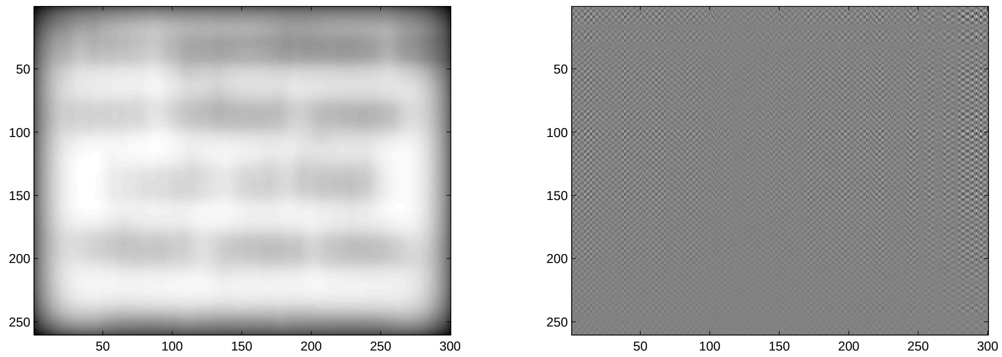

Figure 1.3 *(Left) Recorded blurred image* $b = b_{exact} + b_{noise}$*, [14, Challenge 2]. (Right) Naive solution* $x = A^{+}(b_{exact} + b_{noise})$ *completely dominated by noise.*

$x \in \mathbb{R}^{nm}$ and an optical system (telescope, tomograph, etc.) represented by $A \in \mathbb{R}^{nm \times nm}$ acting upon the input image data x, we obtain a new recorded image $b \in \mathbb{R}^{nm}$. In practice, only the vector b is known and thus the goal is to find the corresponding "model" image x. Assuming A to be linear, the problem can be formulated as

$$A\,x \;=\; b, \tag{1.1}$$

where $A \in \mathbb{R}^{nm \times nm}$, $x \in \mathbb{R}^{nm}$ relates to the wanted model image and $b \in \mathbb{R}^{nm}$ stands for the recorded image.

During recording, transformation of the data leads to addition of redundant information and often blurring of the image occurs. The modification of the data is unavoidable – be it numerical noise caused by the discretization of the problem or impact of inherent physical phenomena (such as gas movements in the atmosphere, motion blur, corrupted / defocussed lens of a recording device, etc.) that corrupts the data. Therefore, the system in question is in fact given by

$$A\,x \;=\; b \;=\; b_{exact} + b_{noise}, \tag{1.2}$$

where A stands for the *blurring operator*, properties of which will be discussed in Section 1.2, and the vectors $b_{exact} \in \mathbb{R}^{nm}$ and $b_{noise} \in \mathbb{R}^{nm}$ are usually unknown.

Using a *pseudoinverse* [1] $A^{+} \in \mathbb{R}^{nm \times nm}$ of the matrix A, we may compute

$$x_{naive} \;\equiv\; A^{+}(b_{exact} + b_{noise}) \;=\; x_{exact} + A^{+} b_{noise}, \tag{1.3}$$

and hence obtain *the least squares solution* to the problem (1.2) (for more details see Section 2.1). As can be seen in Figure 1.3, this operation does not lead to the desired sharp model image x and only yields a naive noise-dominated solution to the problem (i.e. reconstructed image is contaminated by the inverted noise). The reasons why this method cannot be applied to finding a suitable solution will be discussed in Section 1.2.2. Before we do that, let us introduce a deblurring model for colour images.

Colour Images

Construction of a mathematical model describing the blurring process of colour images is slightly more complicated than the one for the gray-scale case. This is a result of the colour images being compounds of three, not just one, 2-dimensional arrays carrying intensity information for different colours, which also implies possible complications during the recording of an image. Specifically, the data assigned to one colour may be infiltrated by different-channel information. Therefore, not only does a colour image suffer from the optical (within-channel) blurring but cross-channel blurring might appear as well (see Figure 1.4 for comparison). Following the same vector notation as above, consider a colour image of the size $n \times m$ pixels: $x = [x^r, x^g, x^b]^T \in \mathbb{R}^{3nm}$, where x^r, x^g, $x^b \in \mathbb{R}^{nm}$ denote the gray-scale images of the three colour channels of x. Assuming the optical blurring (declared by the operator $A : \mathbb{R}^{nm} \to \mathbb{R}^{nm}$) is the same in all three channels, we can write

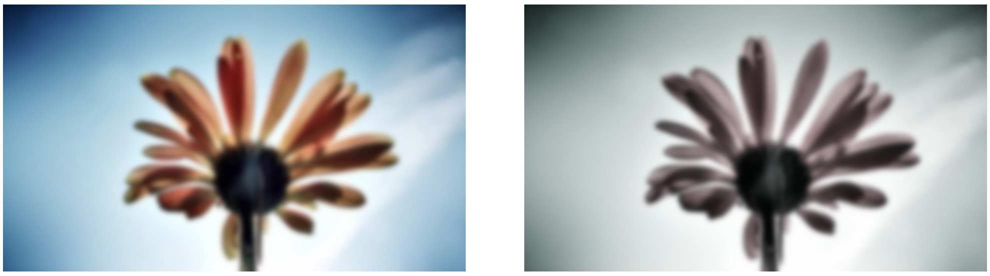

Figure 1.4 *Two types of colour image blurring. (Left) Within-channel blurring. (Right) Within-channel plus cross-channel blurring.*

$$A\,x^r = \tilde{b}^r, \qquad A\,x^g = \tilde{b}^g, \qquad A\,x^b = \tilde{b}^b.$$

The relation between pixel $[\tilde{b}_i^r, \tilde{b}_i^g, \tilde{b}_i^b]^T$ and its cross-blurred counterpart $[b_i^r, b_i^g, b_i^b]^T$ is expressed by

$$\begin{bmatrix} \alpha_{rr} & \alpha_{rg} & \alpha_{rb} \\ \alpha_{gr} & \alpha_{gg} & \alpha_{gb} \\ \alpha_{br} & \alpha_{bg} & \alpha_{bb} \end{bmatrix} \begin{bmatrix} \tilde{b}_i^r \\ \tilde{b}_i^g \\ \tilde{b}_i^b \end{bmatrix} = \begin{bmatrix} b_i^r \\ b_i^g \\ b_i^b \end{bmatrix}, \qquad i = 1, \ldots, nm.$$

Combining the previous two relations [14, pp. 85], the system

$$\begin{bmatrix} \alpha_{rr}A & \alpha_{rg}A & \alpha_{rb}A \\ \alpha_{gr}A & \alpha_{gg}A & \alpha_{gb}A \\ \alpha_{br}A & \alpha_{bg}A & \alpha_{bb}A \end{bmatrix} \begin{bmatrix} x^r \\ x^g \\ x^b \end{bmatrix} = \begin{bmatrix} b^r \\ b^g \\ b^b \end{bmatrix}, \tag{1.4}$$

$[x^r, x^g, x^b]^T$ and $[b^r, b^g, b^b]^T \in \mathbb{R}^{3nm}$, models the colour image blurring problem under the assumption of the spatial invariance of cross-channel blurring, i.e. cross-channel blurring being the same for all pixels. Equivalently, using Kronecker product notation [8, pp. 180], the problem (1.4) can be formulated as

$$(A_{cross-channel} \otimes A)\, x = b, \tag{1.5}$$

with

$$A_{cross-channel} = \begin{bmatrix} \alpha_{rr} & \alpha_{rg} & \alpha_{rb} \\ \alpha_{gr} & \alpha_{gg} & \alpha_{gb} \\ \alpha_{br} & \alpha_{bg} & \alpha_{bb} \end{bmatrix};\ x = \begin{bmatrix} x^r \\ x^g \\ x^b \end{bmatrix},\ b = \begin{bmatrix} b^r \\ b^g \\ b^b \end{bmatrix} \in \mathbb{R}^{3nm}.$$

See Figure 1.4 (Right) for an example of the colour image blurring with $A_{cross-channel}$ =((0.4, 0.35, 0.25), (0.25, 0.2, 0.55), (0.25, 0.25, 0.5)).

The deblurring task is undertaken in compliance with the blurring model – simple within-channel blurring leads to a system of three independent deblurring problems, while occurrence of cross-channel colour blurring requires finding solution to the problem (1.5). Please note that only the first type of problems shall be considered in our numerical experiments in Chapter 3.

1.2 Characteristics of the Blurring Operator

When outlining the basic structure of the linear deblurring model for digital images, we saw that one of the core requirements of the linear deblurring model is that A be known. Hence, the natural question one may ask is how it can be obtained. In this section, we shall take a look at the construction of the blurring operator A. In order to understand the noisy nature of the solution (1.3), we shall examine the properties of A with the help of the singular value decomposition (SVD).

1.2.1 Blurring as a Two Dimensional Convolution Problem

Exploiting the basic formulation of the linear blurring model (1.1), it can be easily seen that the most straightforward way of finding the blurring operator A is computing

$$A\,e_i, = a_i,$$

where $e_i \in \mathbb{R}^{nm}$, and $a_i \in \mathbb{R}^{nm}$ stands for the i-th column of the matrix $A \in \mathbb{R}^{nm\times nm}$. Equivalently, this operation can be seen as recording of an image of a single *point source*. The blurred result of this process, and the function defining the blurring, is then called the **point spread function** (PSF) [14], see Figure 1.5. This experimental approach is often employed in areas such as astronomical imaging or microscopy, where a single bright star or subresolution fluorescent beads [26] respectively can be utilized as the point sources for finding the PSF. Alternatively, precise knowledge of an underlying physical process causing the blurring leads to the explicit formula for the PSF. For example, the atmospheric blur PSF centered at p_{kl} in $P \in \mathbb{R}^{n\times m}$ is modelled by a two-dimensional Gaussian function

$$p_{ij} = \frac{1}{2\pi\sigma_x\sigma_y}\exp\left(-\frac{1}{2}\left(\frac{i-k}{\sigma_x}\right)^2 - \frac{1}{2}\left(\frac{j-l}{\sigma_y}\right)^2\right), \tag{1.6}$$

where standard deviations σ_x, σ_y determine the width of the PSF. Similarly, out-of-focus blur is defined by the PSF of the form

$$p_{ij} = \begin{cases} 1/(\pi r^2), & (i-k)^2 + (j-l)^2 \le r^2, \\ 0, & \text{otherwise}, \end{cases} \tag{1.7}$$

with p_{kl} being the center element and r radius of the PSF. These relations along with the PSF for linear motion blur can be found in [3], [10], [14].

Regarding its properties [14], PSF can be either *spatially invariant* (blurring of each pixel is the same) or *spatially variant*. Often, as shown in Figure 1.5, characteristics of the recording process imply that the PSF is bounded in a region smaller than the dimensions of the picture indicating the local nature of the blurring. Also, if all light is captured in the imaging process, the sum of the pixel values in the PSF is 1 and the blurring process of the original image $X \in \mathbb{R}^{n\times m}$ leading to the blurred image $B \in \mathbb{R}^{n\times m}$ is modelled by a two-dimensional convolution:

$$B = X * PSF.$$

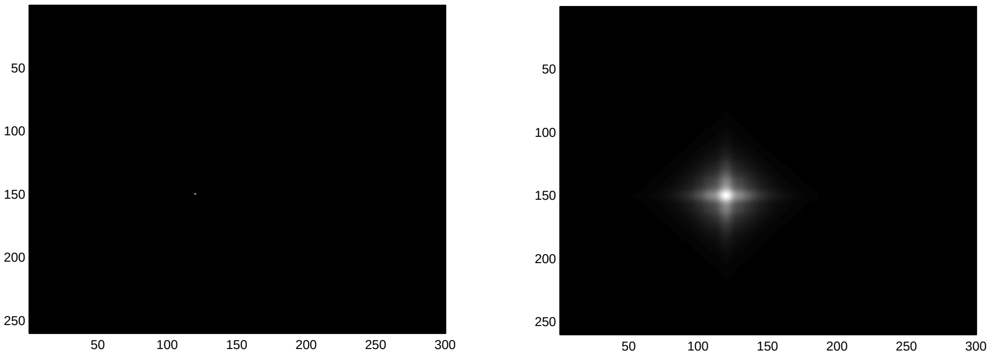

Figure 1.5 *Point source and corresponding point spread function (reshaped into $n \times m$ matrices) for the problem in Figure 1.3.*

In other words, every pixel of the blurred image b_{ij}, $i \leq n$, $j \leq m$ is a weighted average of the corresponding pixel x_{ij} and its neighbours, with the elements of PSF defining the weights for the operation. One should keep in mind that border pixels of B are affected by behaviour of a scene outside of a finite region being recorded. Hence, A needs to be derived from *two* main ingredients: PSF and the **boundary conditions**. When rewriting convolution problem as a matrix-vector multiplication, the choice of the latter to be zero (data outside of X are zero), periodic (periodic extension of the data inside X outwards), or reflexive (outside data being reflection of the data inside X) [5] results in specific block structure of A, namely Toeplitz, circulant, or Hankel, or their combinations. For more details see [14], [25].

1.2.2 Singular Value Decomposition

Singular value decomposition of the operator realizing transformation of an input image data represents a useful tool for understanding the role the inverted noise plays in the problem (1.2). Also, it forms a basis for the methods of the noise elimination in the process of image deblurring.

Consider the singular value decomposition of the matrix $A \in \mathbb{R}^{nm \times nm}$, $rank(A) \equiv r$,

$$A = U \Sigma V^T = \sum_{i=1}^{nm} \sigma_i \, u_i \, v_i^T \,, \tag{1.8}$$

where $U = [\, u_1 \,, \, \ldots \,, \, u_{nm} \,] \in \mathbb{R}^{nm \times nm}$, $V = [\, v_1 \,, \, \ldots \,, \, v_{nm} \,] \in \mathbb{R}^{nm \times nm}$, $U^{-1} = U^T$, $V^{-1} = V^T$,

$$\Sigma = \begin{bmatrix} \Sigma_r & 0 \\ 0 & 0 \end{bmatrix} \in \mathbb{R}^{nm \times nm}, \qquad \Sigma_r = diag(\sigma_1, \, \ldots \,, \sigma_r) \in \mathbb{R}^{r \times r},$$

and $\sigma_1 \geq \sigma_2 \geq \cdots \geq \sigma_r > 0$ are singular values of the matrix A, u_i are left and v_i right singular vectors of the matrix A. For more details and properties of SVD see [8, pp. 70–73].

Expense-wise, the SVD of the matrix A can take on the so-called **economy form**. This way, the unnecessary operations, namely multiplication by zero blocks of Σ in (1.8), are avoided:

$$A \,=\, U_r\,\Sigma_r\,V_r^T \,=\, \sum_{i=1}^{r} \sigma_i\,u_i\,v_i^T\,, \tag{1.9}$$

where $U_r \in \mathbb{R}^{nm\times r}$, $V_r \in \mathbb{R}^{nm\times r}$.

Similarly,

$$\begin{aligned} A^\dagger \; &= \; V_r\,\Sigma_r^\dagger\,U_r^T \,=\, \sum_{i=1}^{r} \frac{u_i^T}{\sigma_i}\,v_i\,, && (1.10) \\ \Sigma_r^\dagger \; &= \; diag(\sigma_1^{-1},\,\ldots\,,\sigma_r^{-1}) \in \mathbb{R}^{r\times r}, \end{aligned}$$

denotes the economy singular value decomposition of a **Moore-Penrose pseudoinverse** [20] of the matrix A. If A is nonsingular, the pseudoinverse and inverse of A coincide. Using this relation, the naive solution to the problem (1.2) can be written as

$$\begin{aligned} x_{naive} \; &= \; \sum_{i=1}^{r} \frac{u_i^T b}{\sigma_i}\,v_i \,= && (1.11) \\ &= \; \sum_{i=1}^{r} \frac{u_i^T b_{exact}}{\sigma_i}\,v_i \,+\, \sum_{i=1}^{r} \frac{u_i^T b_{noise}}{\sigma_i}\,v_i \,= && (1.12) \\ &= \; x_{exact} \,+\, A^\dagger\,b_{noise}, \end{aligned}$$

where the inverted noise $A^\dagger\,b_{noise}$ takes over our naive solution (see Figure 1.3). The explanation for this phenomenon lies in the following properties of image deblurring problems [12], [14]:

- Singular vectors corresponding to small singular values *typically* correspond to higher frequency information – as i increases, left and right singular vectors are apt to have more sign changes (see Figure 1.6).

- The projections $|u_i^T b_{exact}|$ in (1.12) decay on average faster than the corresponding singular values σ_i, and so the reasonable boundedness of the left-hand side sum in (1.12) is ensured, i.e. these coefficients comply with the so called **discrete Picard condition** [12, pp. 82].

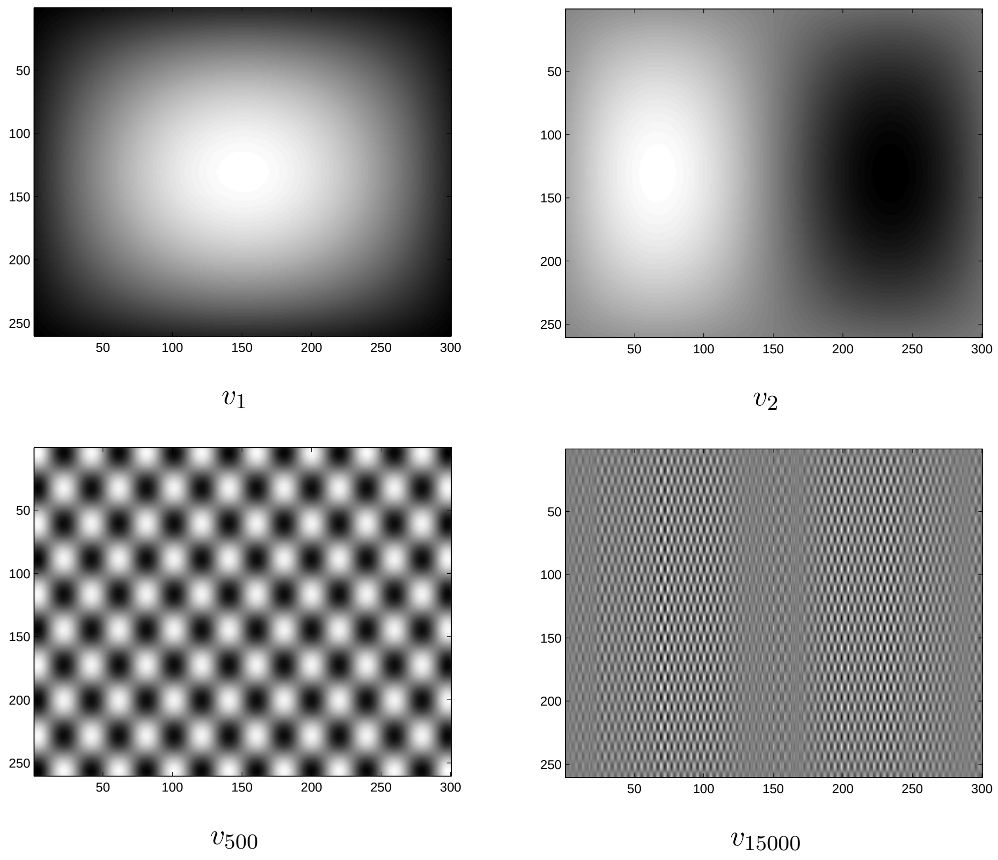

v_1 v_2

v_{500} v_{15000}

Figure 1.6 *Right singular vectors (reshaped into $n \times m$ matrices) corresponding to the blurring operator for the problem in Figure 1.3.*

- On the other hand, noise projections into the left singular subspaces are of a random nature with roughly the same order of magnitude for all $i = 1, \ldots, nm$. This level is known as the **noise level** δ_{noise} and defined by [17]

$$\delta_{noise} \equiv \frac{\|b_{noise}\|}{\|b_{exact}\|},$$

where $\|\cdot\|$ stands for the Euclidean norm $\|\cdot\|_2$. Consequently, as singular values σ_i decay to zero for $i \to nm$, elements $\frac{u_i^T b_{noise}}{\sigma_i}$ grow uncontrollably, the high frequency information is amplified and the discrete Picard condition cannot be satisfied. In other words, the useful image information is entirely suppressed by the inverted noise:

$$\|x_{exact}\| \ll \|A^{\dagger}\, b_{noise}\|.$$

Figure 1.7 shows that magnitude of the projections $|u_i^T b|$ (black)

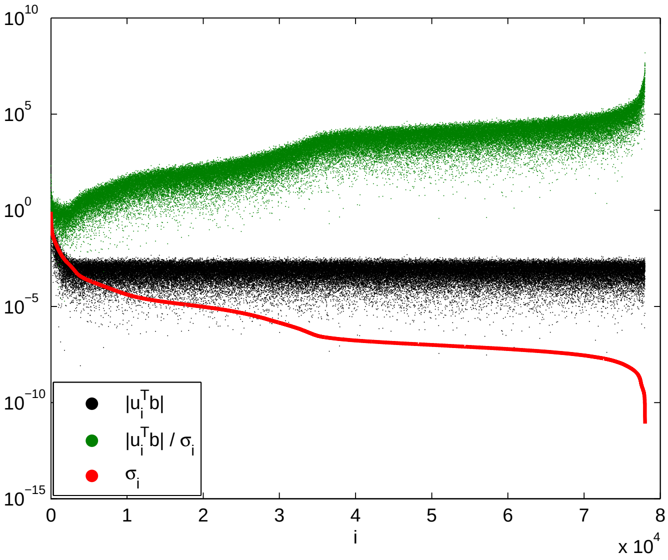

Figure 1.7 *Singular values (red) of the blurring operator A from the problem in Figure 1.3, projections $|u_i^T b|$ (black), and coefficients $\frac{|u_i^T b|}{\sigma_i}$ (green).*

decays at approximately the same rate as the singular values (red) of A before stopping at the noise level δ_{noise}, while growing coefficients $\frac{|u_i^T b_{noise}|}{\sigma_i}$ (green) account for the solution dominated by the elements corresponding to small singular values.

- Singular values of the matrix A decay to, and cluster at, zero which leads to the large condition number $\kappa(A) = \frac{\sigma_1}{\sigma_r}$ and so sensibility of the solution to errors and perturbations.

The last property brings us to the more general characteristic of the image deblurring problems – the one of their *ill-posedness*.

1.2.3 Ill-posed problems

The problem of deblurring images using model (1.2) *often* falls into the group of so called *ill-posed problems*[1] with a very ill-conditioned blurring matrix A. Approaching these problems numerically, one should consider a *numerical ϵ-rank* r_ϵ [8, pp. 72] of the matrix A, which can be

---

[1] The concept of ill and well-posed problems was first introduced by Hadamard. He defined a problem as ill-posed whenever a solution was non-existent, not unique or not continuously dependent on the data – small perturbations in the data bring about arbitrarily large perturbation in the solution [19].

defined by

$$r_\epsilon = \min_{\|A-B\| \le \epsilon} rank(B), \tag{1.13}$$

for a given small tolerance ϵ. In other words, r_ϵ satisfies

$$\sigma_{r_\epsilon} > \epsilon \ge \sigma_{r_\epsilon+1}. \tag{1.14}$$

When looking at the set of singular values of the matrix A, we may distinguish two classes of ill-conditioned problems [12]:

- **Discrete ill-posed problems** – numerical rank of the matrix A is not well-defined, i.e. all singular values of A decay gradually to zero. Numerical treatment of this kind of problems lies in finding a balance between the norm of the solution and the residual norm.
- **Rank-deficient problems** – problems with a well-defined numerical rank r_ϵ characterized by a well-determined gap between the large and small singular values of the matrix A, or as per (1.14), between σ_{r_ϵ} and $\sigma_{r_\epsilon+1}$. This implies the existence of linearly dependent columns / rows of the matrix A and hence the presence of redundant information in the matrix. Thus, linearly dependent information needs to be extracted so that a problem with a well-conditioned matrix could be solved. However, note that r_ϵ needs to be insensitive to small perturbations of ϵ and the singular values. Otherwise, the problem should be dealt with by techniques aimed at discrete ill-posed problems.

Figure 1.8 illustrates these two classes of ill-posed problems: a discrete ill-posed (Left) and rank-deficient problem (Right).

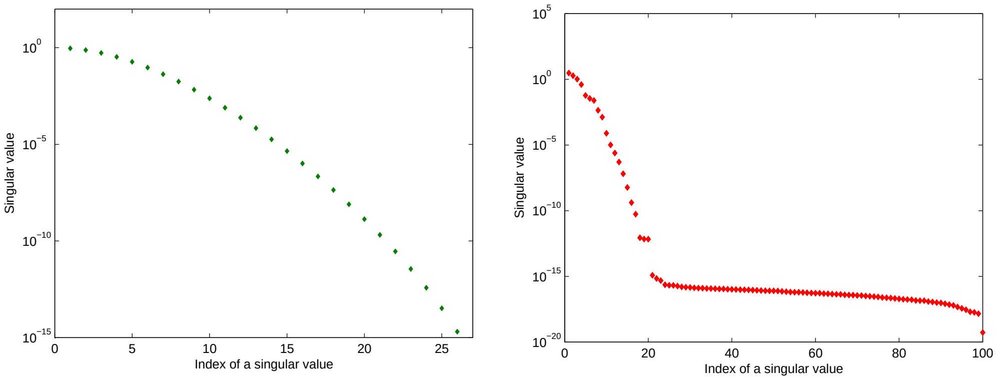

Figure 1.8 *Two examples of the ill-posed problems from the Regularization Toolbox [13]: (Left) Discrete ill-posed problem* Parallax *where singular values gradually decrease to zero. (Right) Rank-deficient problem* Shaw *with a well-determined numerical rank.*

Chapter 2

Numerical Treatment of Image Deblurring Problems

Having discussed the fundamental properties of the image deblurring problems, we see that finding exact (naive) solution to the system (1.2)

$$A\,x \;=\; b \;=\; b_{exact} + b_{noise}$$

does not bring about desirable outcomes. The useful information is suppressed and the noise takes over the resulting image. Therefore, as already indicated, a different approach needs to be taken to deal with these problems. In this chapter, we shall provide a brief overview of the selected numerical techniques aimed at deblurring digital images, namely direct and iterative regularization methods – TSVD, Tikhonov regularization, CGLS, LSQR, and the pertinent stopping criteria (parameter-choice methods) – L-curve, GCV and the discrepancy principle.

2.1 Image Deblurring Methods

Mathematical background of the image deblurring methods presented in this chapter lies in the numerical treatment of the problem (1.2) and the corresponding **linear least squares problem**

$$\min_{x\in\mathbb{R}^{nm}} \|b - A\,x\|. \tag{2.1}$$

Equivalently [4], the least squares solution to (1.2) can be obtained by solving a system of *the normal equations*

$$A^T A\,x \;=\; A^T b, \tag{2.2}$$

with a symmetric nonnegative definite matrix $A^T A \in \mathbb{R}^{nm\times nm}$. We shall benefit from this property later in Section 2.1.2.

2.1.1 Direct Regularization Methods

Direct regularization techniques, as a class of the methods based on the singular value decomposition, stem from the nature of the blurring operator as described in Section 1.2.2. The amplification of the high frequency information due to decaying singular values (Figures 1.7) calls for a way of controlling the role single elements $\frac{u_i^T b}{\sigma_i} v_i$ play in the expansion (1.11).

Using **filter factors** ϕ_i the regularized solution can be defined as

$$x_{filt} = \sum_{i=1}^{r} \phi_i \frac{u_i^T b}{\sigma_i} v_i, \tag{2.3}$$

where $r = rank(A)$ [12, pp. 71–74]. A suitable choice of filter factors, determined by the regularization method, can help dampen the effects of the noise in the wanted model image by muting the information corresponding to the small singular values of A. We shall take a closer look at two of these direct regularization techniques – the truncated singular value decomposition and the Tikhonov regularization.

Truncated Singular Value Decomposition

Truncated singular value decomposition (TSVD) [4], [12], [14] is an elegantly simple yet important representative of the regularization methods class. Here, the filter factors are chosen so that the disturbing elements connected with the small singular values are left out:

$$\phi_i = \begin{cases} 1, & i = 1, \dots, k, \\ 0, & i = k+1, \dots, r. \end{cases}$$

The regularized solution is then of the form

$$x_{TSVD} = \sum_{i=1}^{k} \phi_i \frac{u_i^T b}{\sigma_i} v_i, \tag{2.4}$$

where $k \leq r$ denotes the **truncation level** – a **regularization parameter** of the method regulating the smoothness of the solution (for more details see Section 2.2). The idea behind the TSVD lies in the lower-rank approximations of the matrix A. From the Eckart - Young - Mirsky theorem [8, Theorem 2.5.3], [9], it follows that

$$A_k \equiv \sum_{i=1}^{k} \sigma_i u_i v_i^T, \tag{2.5}$$

$A_k \in \mathbb{R}^{nm\times nm}$ is the best rank-k approximation of the matrix $A \in \mathbb{R}^{nm\times nm}$. Hence the TSVD solves the least squares problem related to (1.2) [4, pp. 101]:

$$\min_{x\in\mathbb{R}^{nm}} \|b - A_k\, x\|.$$

For comparison with the naive solution in Figure 1.3, we include the TSVD solution to the same problem, see Figure 2.1. This solution corresponds to the regularization parameter $k = 2195$.

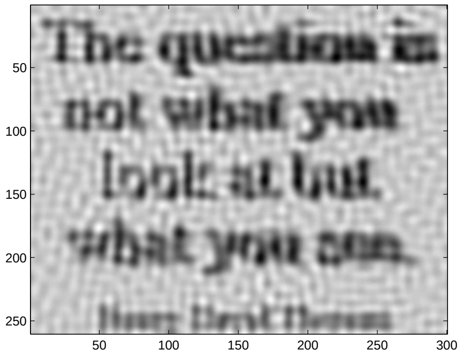

Figure 2.1 *The TSVD solution to the problem in Figure 1.3 with the truncation level $k = 2195$.*

Tikhonov Regularization

Attempts to include apriori assumptions about the properties (size and smoothness) of the solution into the regularization process lead to Tikhonov regularization [4], [12], solving the minimization problem

$$\min_{x\in\mathbb{R}^{nm}} \left\{ \|b - A\,x\|^2 + \lambda^2 \|x\|^2 \right\}, \tag{2.6}$$

with λ standing for the regularization parameter.

Similarly to (2.2), the problem (2.6) is equivalent to solving the modified normal equations

$$(A^T A + \lambda^2 I)\, x \;=\; A^T b.$$

Using the singular value decomposition, the solution to this system can be written as [18]

$$x_{Tikhonov} \;=\; \sum_{i=1}^{r} \frac{\sigma_i^2}{\sigma_i^2 + \lambda^2}\, \frac{u_i^T b}{\sigma_i}\, v_i.$$

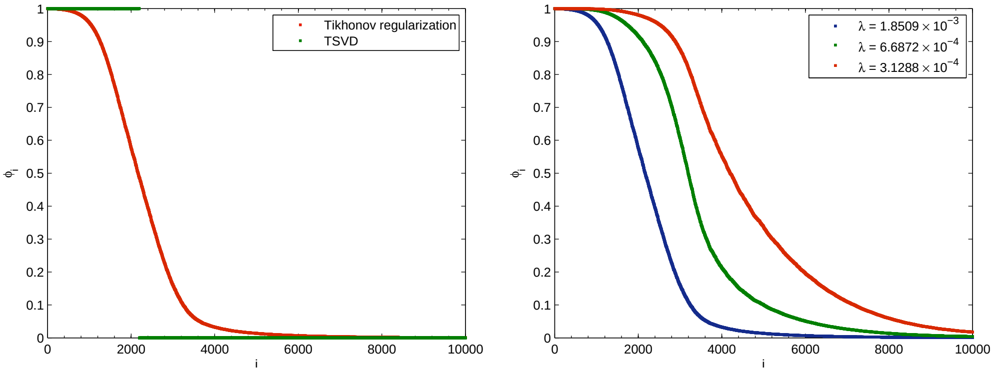

Figure 2.2 *Filter factors corresponding to the problem in Figure 1.3: (Left) Comparison of the ϕ_i for the TSVD solution in Figure 2.1 with $k = 2195$ and the Tikhonov regularization with $\lambda = \sigma_{2195} = 1.8509 \times 10^{-3}$. (Right) Tikhonov factors for different values of λ.*

Hence, the Tikhonov filter factors are given by

$$\phi_i = \frac{\sigma_i^2}{\sigma_i^2 + \lambda^2}, \qquad i = 1, \ldots, r. \tag{2.7}$$

This way both, the residual norm $\|b - A\,x_{filt}\|$ of the discrete ill-posed problem, controlling the smoothness of the solution, and the norm of the solution $\|x_{filt}\|$ can be held reasonably balanced. Taylor expansion of the expression (2.7) reveals that $\phi_i \approx 1$ for $\sigma_i \gg \lambda$, and $\phi_i \approx \sigma_i^2/\lambda^2$ for $\sigma_i \ll \lambda$, suggesting that Tikhonov filters set in effectively when $\sigma_i \approx \lambda$, see [14, pp. 70].

Figure 2.2 illustrates the first 10000 filter factors (out of 78000) for the regularization of the problem in the Figure 1.3. See figure on the left for comparison of the Tikhonov and TSVD filter factors ϕ_i. Right figure illustrates the Tikhonov factors for different values of λ.

2.1.2 Iterative Regularization Methods

Both iterative techniques outlined in this section, CGLS and LSQR, take advantage of the conjugate gradients method (CG) [16] and project a large problem (1.2) onto a Krylov subspace of the smaller dimensions [4], [8], [12]. The CG algorithm applied to the normal equations (2.2) can either lead to CGLS, or LSQR, if implemented via Golub - Kahan bidiagonalization [21]. Although these methods are *mathematically* equivalent they do exhibit different properties when implemented in the finite arithmetics [12].

CGLS

The CGLS is a Krylov subspace method [4, Section 7.4.1] with the iterated solution x_k minimizing the error functional

$$\mathcal{F} = (\bar{x} - x_k)^T A^T A\, (\bar{x} - x_k),$$

over the affine subspace $x_0 + \mathcal{K}_k(A^T A,\, A^T(b - A\, x_0))$, for a given starting vector x_0 and $\bar{x} = A^\dagger b$ being the least squares solution (1.3). The algorithm is initialized with x_0, $r_0 = b - A\, x_0$, $p_0 = A^T r_0$ and executed for $k = 1, 2, \ldots$

$$\begin{aligned} \alpha_k &= \|A^T r_{k-1}\|^2 \,/\, \|A\, p_{k-1}\|^2, \\ x_k &= x_{k-1} + \alpha_k\, p_{k-1}, \\ r_k &= r_{k-1} - \alpha_k\, A\, p_{k-1}, \\ \beta_k &= \|A^T r_k\|^2 \,/\, \|A^T r_{k-1}\|^2, \\ p_k &= A^T r_k + \beta_k\, p_{k-1}. \end{aligned}$$

Here the vector r_k denotes k-th residual vector $r_k = b - A\, x_k$, and p_k is an auxiliary vector. For more details and convergence properties see [4], [6], [16].

LSQR

The LSQR algorithm [22] is based on the *Golub - Kahan bidiagonalization* [21] and can be implemented as follows. For a given initial vector $u_1 = b/\beta_1$, where $\beta_1 = \|b\| \neq 0$, and $v_0 = 0$ the loop computes for $i = 1, 2, \ldots$

$$\begin{aligned} \alpha_i\, v_i &= A^T u_i - \beta_i\, v_{i-1}, \qquad \|v_i\|, &= 1, \\ \beta_{i+1}\, u_{i+1} &= A\, v_i - \alpha_i\, u_i, \qquad \|u_{i+1}\|, &= 1, \end{aligned} \tag{2.8}$$

until $\alpha_i = 0$ or $\beta_{i+1} = 0$, or until $i = nm$. The recurrence (2.8) may then be rewritten into the matrix form as

$$\begin{aligned} A^T U_{k+1} &= V_k\, L_{k+}^T + \alpha_{k+1}\, v_{k+1}\, e_{k+1}^T, \\ A\, V_k &= U_{k+1}\, L_{k+}, \end{aligned}$$

where $U_{k+1} = (u_1, \ldots, u_{k+1}) \in \mathbb{R}^{nm \times (k+1)}$, $V_k = (v_1, \ldots, v_k) \in \mathbb{R}^{nm \times k}$ are orthonormal matrices and $L_{k+} \in \mathbb{R}^{(k+1) \times k}$ stands for a lower bidiagonal matrix

$$L_{k+} = \begin{bmatrix} \alpha_1 & & & \\ \beta_2 & \alpha_2 & & \\ & \ddots & \ddots & \\ & & \beta_k & \alpha_k \\ & & & \beta_{k+1} \end{bmatrix}.$$

Hence [4] we have $\mathrm{span}(U_k) = \mathcal{K}_k(A\,A^T,\, b)$, $\mathrm{span}(V_k) = \mathcal{K}_k(A^TA,\, A^Tb)$. The algorithm then seeks the approximate solution $x_k \in \mathcal{K}_k(A^TA,\, A^Tb)$, by taking $x_k = V_k\, y_k$, with $y_k \in \mathbb{R}^k$ minimizing the k-th residual

$$r_k \;=\; b - A\,x_k \;=\; \beta_1\, u_1 - A\,V_k\, y_k \;=\; U_{k+1}\,(\beta_1\, e_1 - L_{k+}\, y_k).$$

In other words, the LSQR projects the problem (1.2) onto a lower-dimensional Krylov subspace [4, pp. 307] resulting in

$$L_{k+}\, y_k \;\approx\; \beta_1\, e_1,$$

and in each step it solves the corresponding linear least squares problem

$$\min_{y_k \in \mathbb{R}^k} \|L_{k+}\, y_k - \beta_1\, e_1\|.$$

More about the LSQR algorithm, its convergence rates and finite-arithmetics implementation issues can be found in [4], [12], [22], [23].

2.2 Stopping Criteria

In the previous section, we have summarized several ways of approaching the image deblurring problems by means of regularization. As suggested above, the success of these methods depends on a good pick of the regularization parameter, namely λ for Tikhonov regularization or k for TSVD, and also CGLS and LSQR.

To illustrate the importance of this choice, we present an example of deblurring via the TSVD for different values of the truncation parameter k, see Figure 2.3. Notice that for a small value of the regularization parameter, $k = 1000$, the solution is free of errors, the data are not polluted by noise. However, the lack of the useful information leads to an *overregularization* and indistinct results. By increasing k to the value of 30000, we obtain a more desirable solution. Incrementing further, not only do we add more information, but we also contaminate the solution by the high frequency elements corresponding to the small singular values. This situation of *underregularization* is depicted for $k = 40000$ and $k = 75000$. We see that for large values of the regularization parameter, the solution is completely overtaken by the inverted noise.

Changes of regularization parameters pertinent to other methods in question bring about similar situations. Large values of λ for the Tikhonov regularization and small values of k for LSQR and CGLS lead to the overregularization, while decreasing λ and increasing k end up

Exact image *Blurred image*

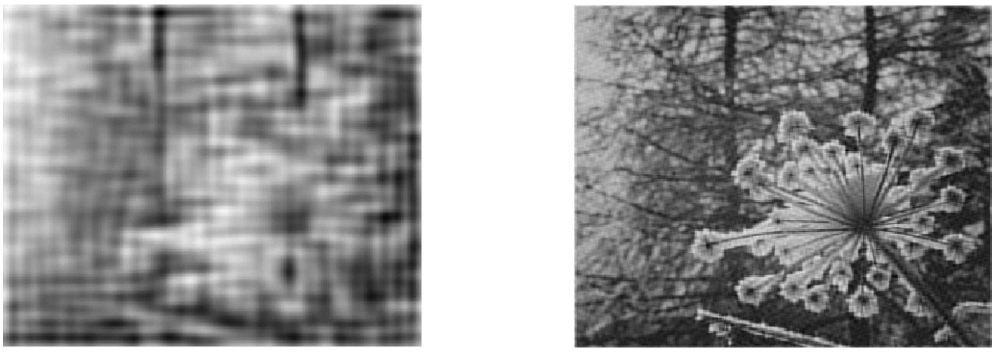

$k = 1000$ $k = 30000$

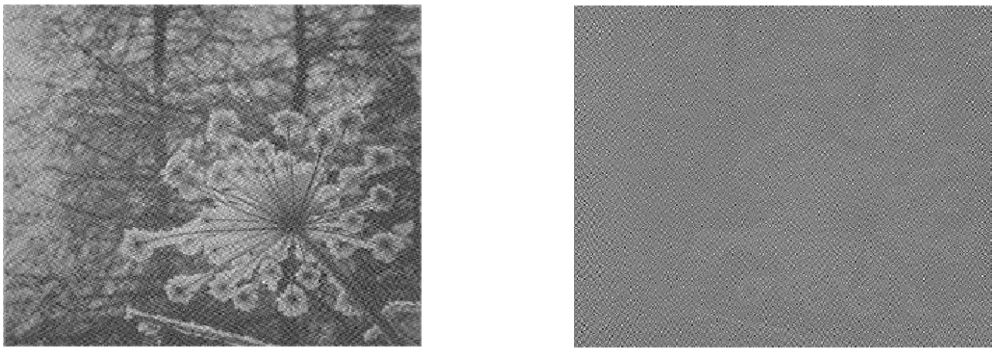

$k = 40000$ $k = 75000$

Figure 2.3 *Original and blurred image and the TSVD solutions for different values of the regularization parameter* k.

in the underregularization of the solution. Thus, it can be seen that a suitable choice of the regularization parameter is crucial for obtaining desirable results.

Mathematically speaking, consider the exact solution $x_{exact} = A^{\dagger}\, b_{exact}$ and its regularized counterpart $x_{filt} = A^{\sharp}\, b$, where $A^{\sharp}$ stands for a *regularized inverse* of the matrix A (e.g. $A^{\sharp} = A_k^{+}$ for the TSVD, with A_k from (2.5)). Then

$$\begin{aligned} x_{exact} - x_{filt} &= A^{\dagger}\, b_{exact} - A^{\sharp}\, b = \\ &= (A^{\dagger} - A^{\sharp})\, b_{exact} - A^{\sharp}\, b_{noise}, \end{aligned}$$

and the decision about the value of the regularization parameter lies in balancing *the regularization error* $\|(A^{\dagger} - A^{\sharp})\, b_{exact}\|$ and *the perturbation error* $\|A^{\sharp}\, b_{noise}\|$ in order to minimize the total error [12, pp. 176]. The change of the regularization parameter influences the trade-off between these two values: the more regularization is introduced into the problem, the bigger the regularization error yet smaller the perturbation one, and vice versa.

Applying the TSVD to the ill-posed problems with a well determined numerical rank (rank-deficient problems, see Section 1.2.3), one may opt for choosing the regularization parameter equal to this value. This way, the unnecessary loss of useful information and consequent increase in the regularization error is avoided. Also, this choice leads to a cutback of the perturbation error due to exclusion of the noise elements corresponding to small singular values from the solution and is independent of the right-hand side [12, Section 7.1].

However, in the discrete ill-posed case, it is much more difficult to achieve the balance between the two errors. Depending on the information available, we differentiate between two classes of parameter-choice methods:

- Methods working with the given right-hand side b in (1.2) to extract the relevant information about the noise in the data, e.g. **the L-curve** and **the Generalized Cross Validation**.

- Methods based on the a priori knowledge of the noise level, i.e. exact value or a good estimate of $\|b_{noise}\|$. **The discrepancy principle** can be considered the most common representative of this class.

We shall now discuss the three methods in more detail.

2.2.1 L-curve

The L-curve, as a parameter-choice method for the ill-posed problems, is a log-log plot of the norm of the regularized solution $\|x_{filt}\|$ versus the corresponding residual norm $\|b - A\,x_{filt}\|$. The method, primarily developed to complement the Tikhonov regularization, has been studied extensively by Hansen and O'Leary [11], [12], [15] and has found wider application in other techniques as well.

The L-curve can be either continuous, in case of the continuous regularization parameter such as λ in Tikhonov regularization, or composed of the discrete set of points for regularization methods with a discrete regularization parameter k. The basic assumption for the use of the L-curve is the monotonicity of the residual norm and the norm of the solution [12]. Often, as in Figure 2.4 (Left) depicting the TSVD L-curve for the problem in Figure 2.3, the curve takes on the L-shape, which facilitates the computations. Nevertheless, it is worth noting that this is not always the case, see Figure 2.4 (Right). Trying to balance the two norms, the L-curve aims at finding the regularization parameter preventing the *oversmoothing* (situation corresponding to the rightmost part of the L-curve) and *undersmoothing* (uppermost part of the L-curve) of the solution. Intuitively, the most suitable parameter should lie at the "corner" of the curve. Note that the rightward movement along the curve coincides with an increase of λ and decrease of k, while moving leftwards reflects a reverse situation.

Hence, the task to find the suitable regularization parameter is transformed into the problem of finding the point of the maximum curvature on the curve, [15]. More precisely, given the parametric definition of the L-curve

$$(\zeta(p), \eta(p)) \;=\; (\log\|b - A\,x_{filt}\|,\, \log\|x_{filt}\|),$$

where $p = \lambda$ for the Tikhonov regularization, or $p = k$ for TSVD, CGLS or LSQR, we seek a regularization parameter p, for which the curvature

$$\kappa(p) \;=\; \frac{\zeta'\eta'' - \zeta''\eta'}{((\zeta')^2 + (\eta')^2)^{3/2}}$$

is maximized. However, note that the computation requires a twice differentiable smooth curve. Thus, in the discrete case, Hansen and O'Leary propose fitting a cubic spline to the points of the L-curve. For further details on the properties and computational aspects of the L-curve see [2], [11], [12], [15].

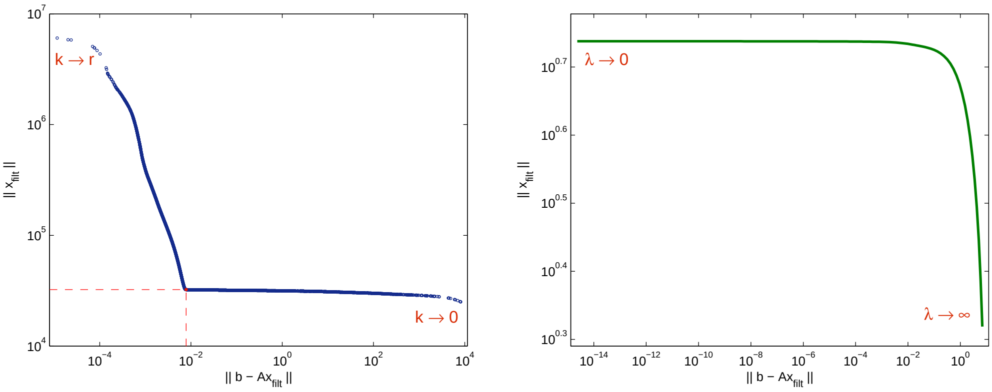

Figure 2.4 *(Left)L-curve for the TSVD of the problem in Figure 2.3 with a corner at* $k = 31147$. *(Right) L-curve for the Tikhonov regularziation of the problem* Shaw(30) *from the Regularization Toolbox [13].*

2.2.2 Generalized Cross Validation

The Generalized Cross Validation (GCV) represents a parameter-choice method based on statistical ideas. The GCV suggests that a suitable regularization parameter should lead to a solution capable of correctly predicting data values that have been omitted from the right-hand side b [12, Section 7.4]. To do this, one seeks to minimize the GCV functional

$$\mathcal{G}(p) = \frac{\|b - A\,x_{filt}\|^2}{(trace(I_{nm} - A\,A^{\sharp}))^2}$$

where $p = \lambda$ for the Tikhonov regularization, or $p = 1/k$ for TSVD, CGLS or LSQR. Figure 2.5 illustrates the GCV function for the first two techniques. Provided suitable characteristics of the regularization method, the general form of $\mathcal{G}(p)$ can be further simplified, e.g. for the TSVD we have [14]

$$\mathcal{G}(k) = \frac{\|b - A\,x_k\|^2}{(nm - k)^2} = \frac{1}{(nm - k)^2} \sum_{i=k+1}^{nm} (u_i^T b)^2.$$

Despite its wide applicability, one of the drawbacks of this method are revealed when dealing with the GCV function ”flat” around its minimum – specifically, numerical difficulties connected with the minimization resulting in under- or oversmoothing of the solution. For deeper understanding see [7], [12], [28].

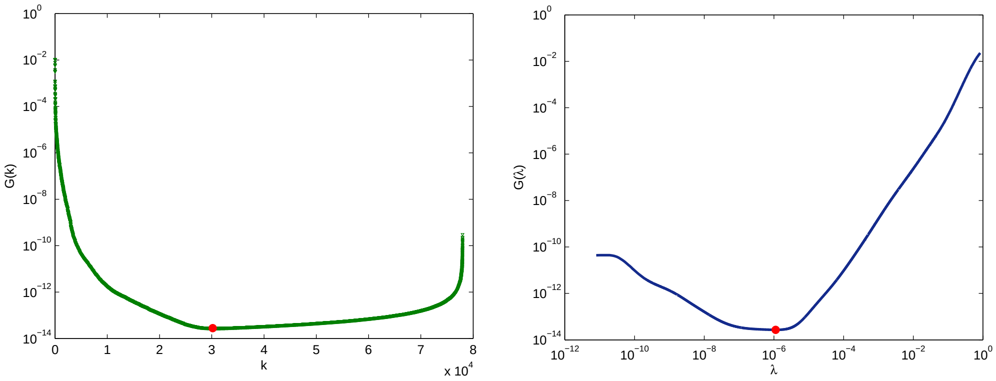

Figure 2.5 *GCV function for the problem in Figure 2.3: (Left) GCV function* $\mathcal{G}(k)$ *with minimum at* $k = 30169$*. (Right) GCV function* $\mathcal{G}(\lambda)$ *with minimum at* $\lambda = 1.1198 \times 10^{-6}$.

2.2.3 Discrepancy principle

Discrepancy principle is the most commonly used $\|b_{noise}\|$-based method of determining the value of the regularization parameter. Building on the a priori knowledge of the noise level, the discrepancy principle chooses such parameter that the residual norm is equal to the known upper bound δ for $\|b_{noise}\|$, [12, Section 7.2]:

$$\|b - A\,x_{filt}\| \;=\; \delta, \qquad \text{where} \qquad \|b_{noise}\| \;\leq\; \delta. \tag{2.9}$$

In discrete situations, the regularization parameter is selected as the smallest k for which $\|b - A\,x_{filt}\| \leq \delta$. Note that the regularized solution x_{filt} corresponds to the point of intersection of the L-curve and the vertical line given by (2.9), and $x_{filt} \to x_{exact}$, as $\delta \to 0$ [14]. Generalization of the concept as well as the statistical properties are further discussed in [12], [18].

Chapter 3

Numerical Experiments

In this chapter we shall present numerical experiments testing previously discussed numerical techniques for digital image processing. The computations were carried out on an Intel(R) Core(TM)2 Duo laptop with CPU T6600 2.20 GHz / 3 GB RAM and the unit roundoff was $\epsilon = 1.2 \times 10^{-16}$. We have worked in MATLAB R2009b and used subroutines from the HNO functions package (supplementary material to [14]) and the Regularization Toolbox [13] that we modified to work for the *separable blur*[1].

Problem 1

The first experiment demonstrates the role of the boundary conditions in the construction of the blurring operator from the point spread function. To blur the original image X of the size 260×549 pixels in Figure 3.1 (Top), we have created a Gaussian blur point spread function with standard deviations $\sigma_x = \sigma_y = 6$, see Section 1.2.1. The resulting PSF was then coupled with different types of boundary conditions and applied to the image.

Figure 3.1 compares the results of the blurring with zero, periodic and reflexive boundary conditions (top to bottom). As the second image suggests, the use of the *zero boundary conditions* leads to the occurrence of the artificial dark edges. This is caused by the fact that a scene outside the exact image is treated as black, the border pixels of X are convolved with zero elements which results in the infiltration of the inside data. On the other hand, *periodic boundary conditions* consider a scene outside of

---

[1] Situation when blurring of the rows is independent of the blurring of the columns of the image. Here, the blurring operator A is expressed by $A = A_r \otimes A_c$, where $A_r \in \mathbb{R}^{m \times m}$ denotes the row blurring and $A_c \in \mathbb{R}^{n \times n}$ the column blurring operator. For more details see [14].

Figure 3.1 *Gaussian blur with different boundary conditions imposed on the exact image. From top to bottom: exact image, blurred images using zero, periodic and reflexive boundary conditions.*

the exact image periodically filled with the exact image data X. This implies that the border data at top / left of the exact image shall influence the blurring of the data at the bottom / right of the image. This can be seen in the third figure – notice the dark edge at the top of the image and lighter edge at the bottom. The *reflexive boundary conditions* avoid the previous artificial effects by reflecting the data inside X outsides. In other words, the pixels in the border area of the image are not affected by any other information, see Figure 3.1 (Bottom).

Hence, we can conclude that each type of the boundary conditions has its specifications which should be considered in order to obtain desirable results.

Problem 2

Problem 2 examines the influence of the noise amount in the image data on the success of the deblurring of an discrete-ill posed problem. The testing blurred image (Figure 3.2 (Left), Gaussian blur with $\sigma_x = \sigma_y = 3$) of the size 196×295 pixels was corrupted by addition of a random noise of three different orders. More precisely, we have constructed three testing images b_1, b_5 and $b_{10} \in \mathbb{R}^{nm\times 1}$, $n = 196$, $m = 295$, corresponding to the noise levels $\delta_{noise} = 10^{-1}$, 10^{-5} and 10^{-10} respectively. The experiment uses the TSVD and compares the results for different values of the regularization parameter k.

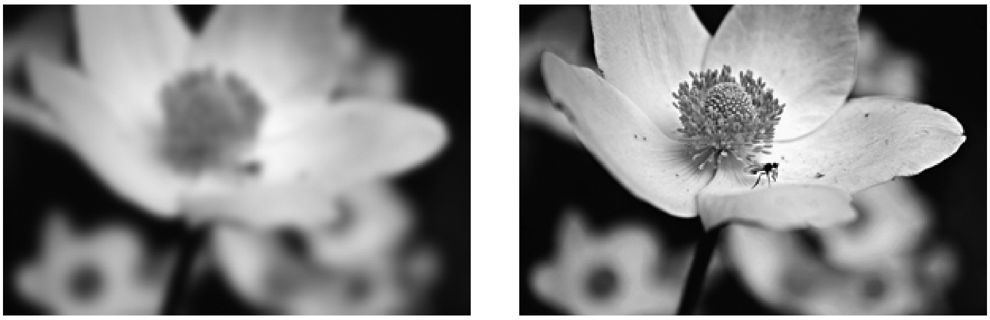

Figure 3.2 *Testing blurred image (Left) and its exact counterpart (Right).*

Figure 3.3 reveals a severe ill-conditioning of the blurring operator A – the order of magnitude of the condition number $\kappa(A) = \sigma_1/\sigma_{nm}$ is 10^{-35}, suggesting that even small perturbations of the data will bring about dramatically large perturbations of the solution. The problem is ill-posed and the blurring operator does not have a well-defined numerical rank, since the singular values decay gradually to zero. The truncation

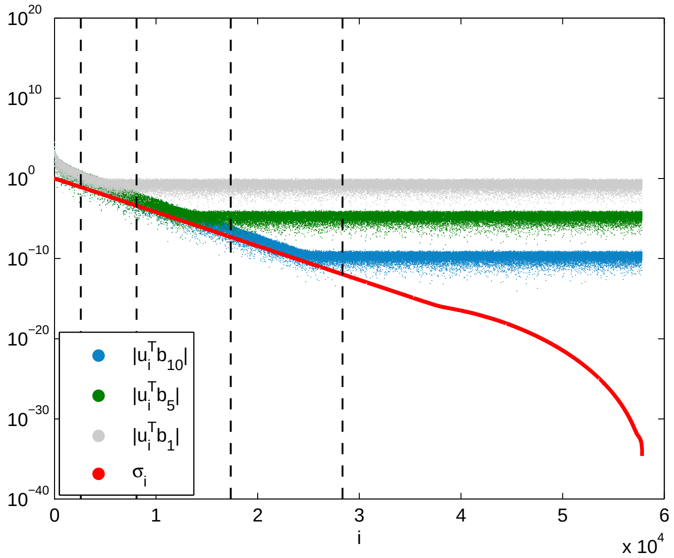

Figure 3.3 *The singular values of the blurring operator and projections* $|u_i^T b_1|$, $|u_i^T b_5|$ *and* $|u_i^T b_{10}|$. *The dashed lines mark the truncation levels of the TSVD:* $k = 2604, 8084, 17350, 28350$.

levels for the experiments were set to $k = 2604$, 8084, 17350, 28350, and are marked by the dashed lines allowing us to estimate the amount of noise information (corresponding to the projections $|u_i^T b_j|$, $j = 1$, 5, 10) that shall leak into the solution. The results of the experiment are presented in Figure 3.4. Notice that as k grows (from top to bottom), the solutions change from over- to underregularized. The situation is the gravest in the case of $\delta_{noise} = 10^{-1}$, where already the choice of $k = 17350$ leads to suppression of any useful image information in the image (Left). It can be seen that the solutions corresponding to $\delta_{noise} = 10^{-10}$ are the most resistant to degradation due to noise. Even for $k = 28350$ one might observe only a slight underregularization.

The experiment shows that in image deblurring of the discrete ill-posed problem, the noise level determines how much information can be included in the solution before it is taken over by the inverted noise. Regarding TSVD, higher levels of noise require smaller values of the regularization parameter, while small noise levels enable choice of larger k and hence inclusion of larger amount of the useful data into the solution.

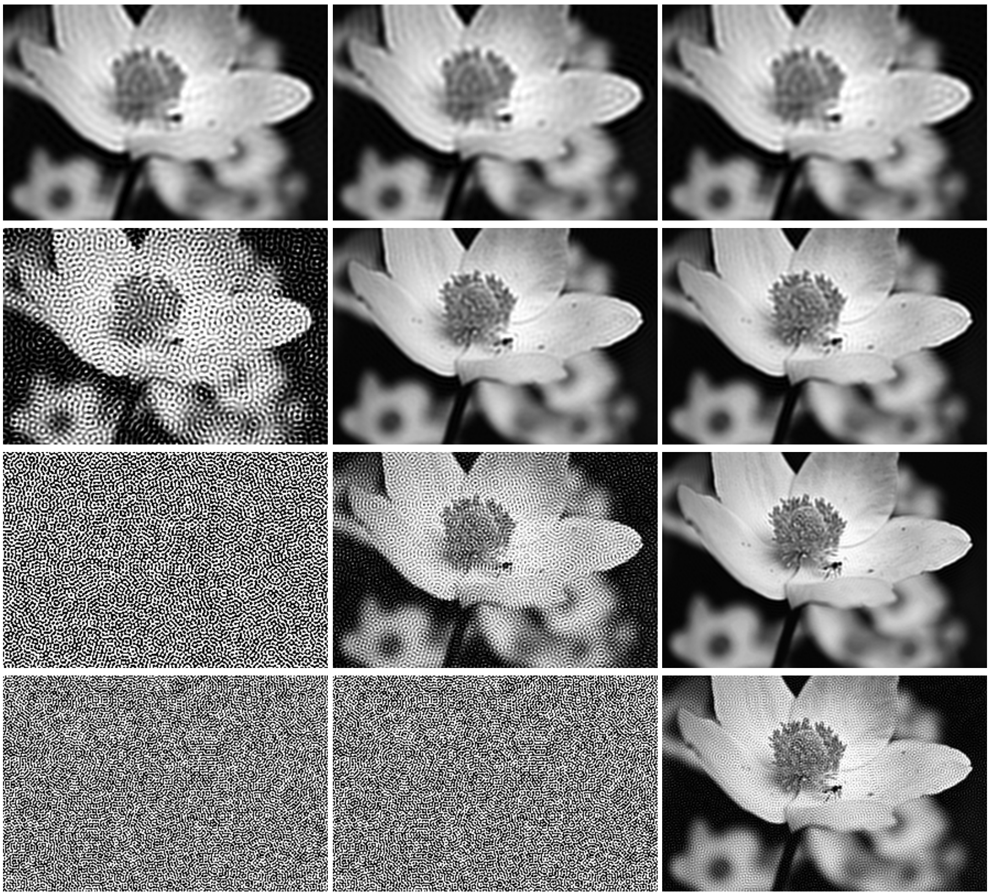

Figure 3.4 *TSVD solutions for different noise and truncation levels. From left to right:* $\delta_{noise} = 10^{-1}$, 10^{-5}, 10^{-10}*. From top to bottom:* $k = 2604$, 8084, 17350, 28350.

Problem 3

The third experiment compares the regularization methods described in Section 2.1 while working on real-life astronomic data. The testing image of Mars craters of the size 222 × 219 pixels, courtesy of NASA/JPL-Caltech [24], was blurred with Gaussian blur with $\sigma_x = \sigma_y = 4$, to simulate the image degradation by the atmospheric blur, and further corrupted by the addition of the random noise with $\delta_{noise} = 10^{-1}$, see Figure 3.5 (Top left).

Using the L-curve criterion for choosing the regularization parameter, we have constructed Tikhonov, TSVD, CGLS and LSQR solutions. Figure 3.5 (Top right, Middle) shows that in this setting, only the Tikhonov regularization provides a desirable solutions. All three other methods exhibit undersmoothing, with the LSQR solution being unacceptably underregularized. The explanation for this lies in the choice of the regularization parameter by the L-curve. Figure 3.6 depicts the L-curves for the four methods. Note that all curves are distinctively L-shaped with well-defined corners, and we display the zoomed plots of these corners only. In case of the TSVD, the use of the L-curve does not lead to the balance of the perturbation and regularization errors. As for the iterative methods, the algorithm[2] failed to localize the true corner of the L-curve, which demonstrated itself drastically for the LSQR.

Since the results provided by the regularization methods are greatly dependent on the parameter-choice method employed, we should avoid their explicit comparison judging solely on this example. To illustrate this, we include the TSVD, CGLS and LSQR solutions to the problem for values of k different from the ones supplied by the L-curve, see Figure 3.5 (Bottom). Notice that these provide better approximations of the exact image.

---

[2] Subroutine *l_corner* from the Regularization Toolbox [13].

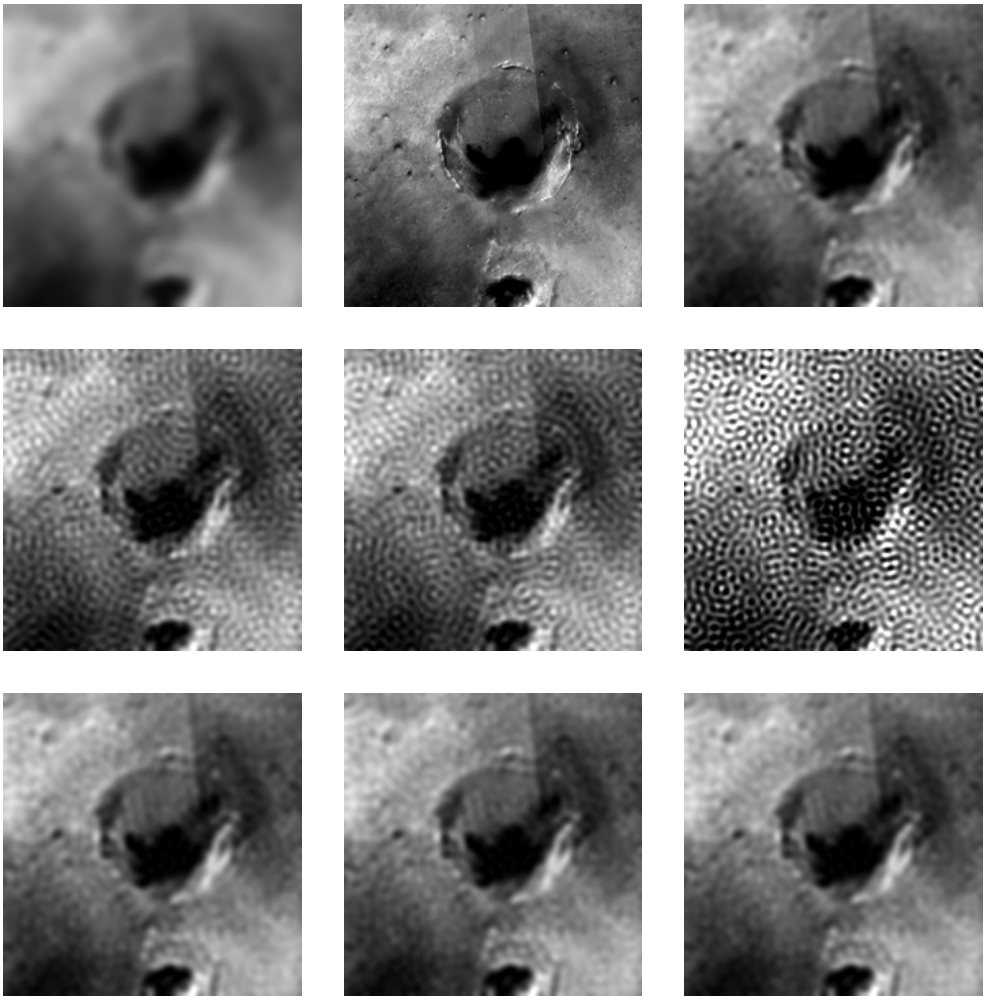

Figure 3.5 *Comparison of the solutions obtained by different regularization methods. From left to right: (Top) Blurred image, original image, Tikhonov solution for* $\lambda = 2.4348 \times 10^{-3}$*, (Middle) TSVD, CGLS and LSQR with* $k = 3095, 490, 7979$ *respectively. Parameters* λ *and* k *were given by the L-curve. (Bottom) The choice of* $k = 2400, 150, 200$ *for TSVD, CGLS and LSQR respectively leads to more desirable results.*

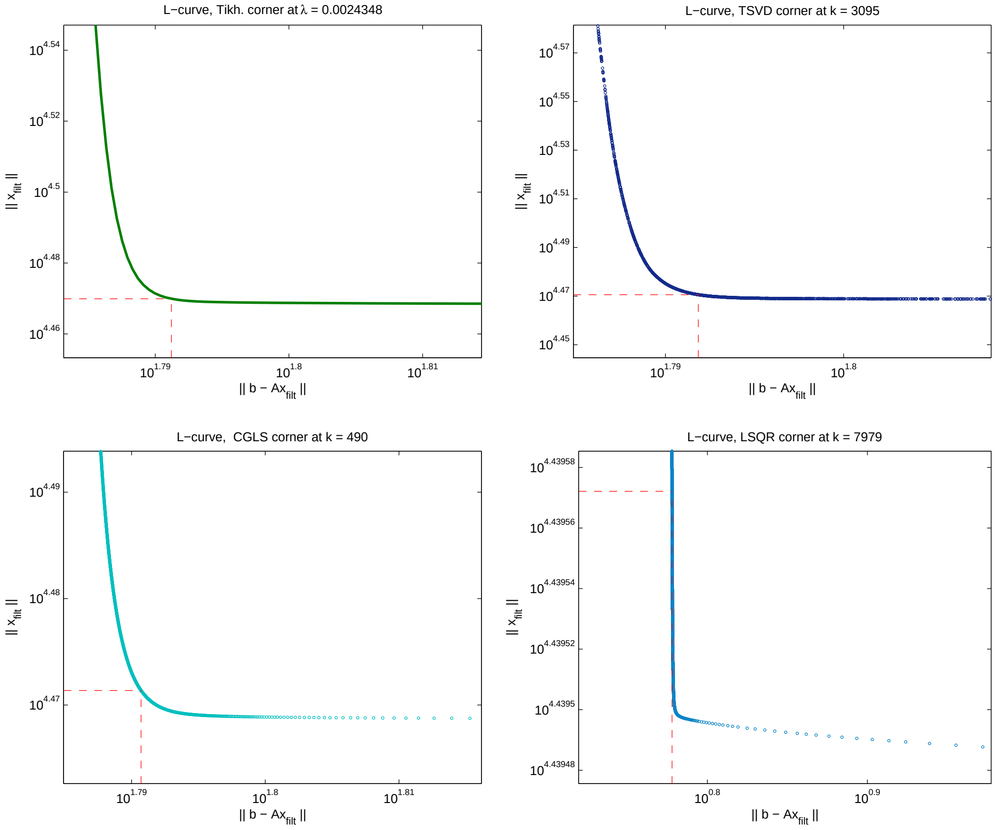
L−curve, Tikh. corner at λ = 0.0024348

L−curve, TSVD corner at k = 3095

L−curve, CGLS corner at k = 490

L−curve, LSQR corner at k = 7979

Figure 3.6 *Corner parts of the L-curves for Tikhonov regularization, TSVD, CGLS and LSQR pertinent to the problem in Figure 3.5.*

Problem 4

In this experiment, we demonstrate a medical application of the numerical techniques in question and compare the results obtained for different parameter-choice methods applied to the Tikhonov regularization. The testing retinal image in Figure 3.8 (Top left) was obtained from the exact image of the size 287×288 pixels taken from the DRIVE database (Digital Retinal Images for Vessel Extraction, [27]) that has been modified by the out-of-focus blur with the radius of 3 pixels, see Section 1.2.1, and addition of the random noise with $\delta_{noise} = 10^{-1}$. Consequently, the white mask has been reapplied to the image to discard the irrelevant data outside of the retinal area.

We have tested all of the three parameter-choice methods presented in the Section 2.2: L-curve, GCV and the discrepancy principle. The L-curve (Figure 3.7, Left) determines the value $\lambda = 1.3717 \times 10^{-5}$, GCV (Right) chooses $\lambda = 0.0052$ and the discrepancy principle $\lambda = 0.0125$. Notice that the corner of the curve is not well-defined and the L-curve-determined parameter is of the smaller order of magnitude compared to the other two, which brings doubts about the accuracy of this choice.

The reconstructed image (Figure 3.8, Top right) confirms this expectation by showing that the L-curve-based solution suffers from high amounts of noise information. Solutions gained via GCV and discrepancy principle can be considered acceptable, with the GCV providing a slightly smoother appearance.

In this example, the GCV turned out to be the most suitable method of ascertaining the value of the regularization parameter. Nevertheless,

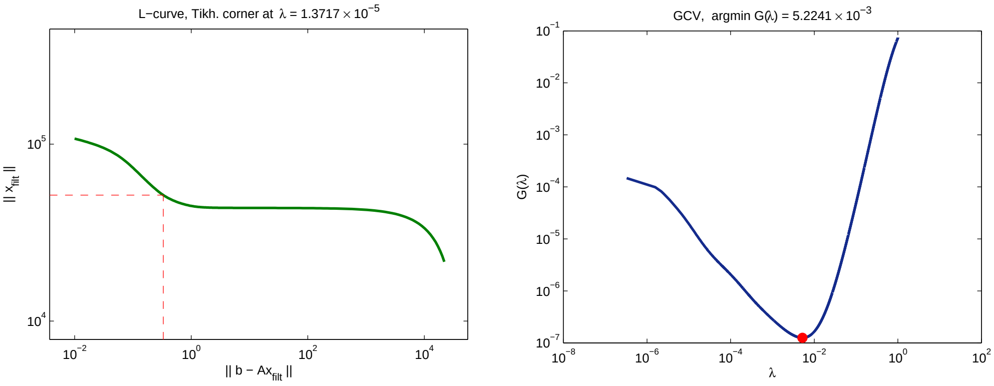

Figure 3.7 *Parameter-choice methods for the Tikhonov regularization of the image in Figure 3.8: (Left) L-curve, notice the indistinct corner of the curve. (Right) GCV function $\mathcal{G}(\lambda)$.*

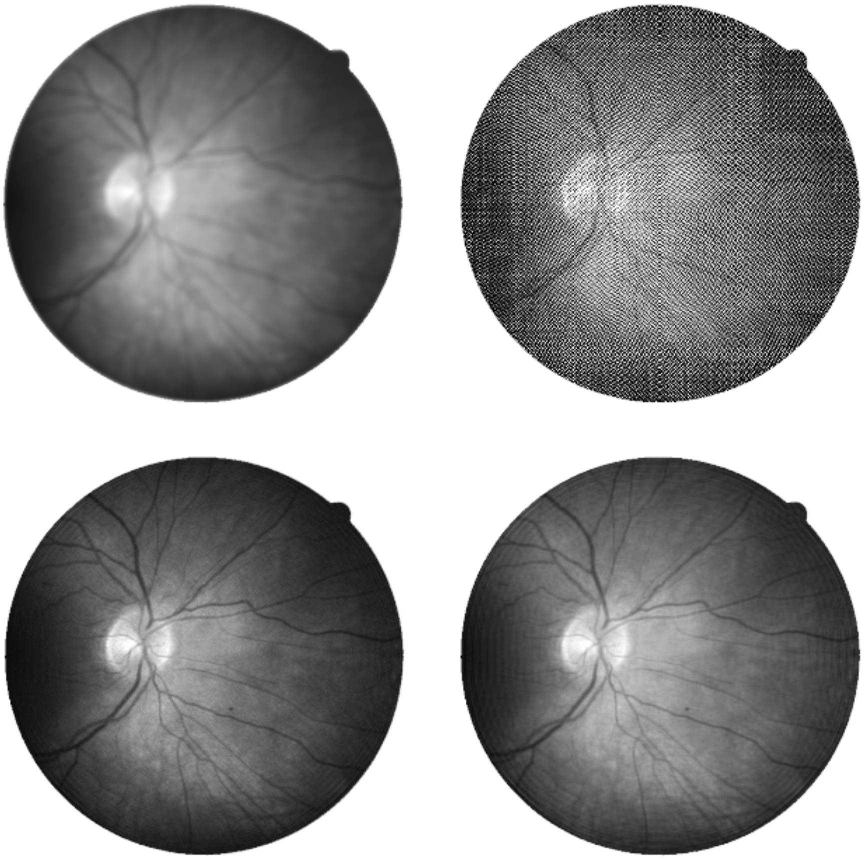

Figure 3.8 *Comparison of the testing image and regularized Tikhonov solutions for different parameter choice methods. From left to right: (Top) Testing retinal image, solution based on L-curve* $\lambda = 1.3717 \times 10^{-5}$*, (Bottom) GCV* $\lambda = 5.2241 \times 10^{-3}$ *and discrepancy principle* $\lambda = 1.25 \times 10^{-2}$.

this does not apply its universal superiority. The feasibility of the methods depends on the particular input image data and the regularization techniques employed.

Problem 5

Problem 5 illustrates deblurring of the colour image with within-channel blurring. To simulate the effects of the defocussed lens of the camera, the blurred image of the size 260 × 391 pixels used for the experiment was obtained as a result of out-of-focus blurring with the radius of 3 pixels and corrupted by random noise with $\delta_{noise} = 10^{-2}$.

Figure 3.9 *Colour image deblurring. (Left) Blurred image, (Right) Tikhonov GCV-based solution. From top to bottom: colour image, gray-scale images corresponding to the red, green and blue channels.*

To restore the image, we have used the Tikhonov regularization, while the value of the regularization parameter was provided by the GCV. Figure 3.9 demonstrates that in order to deblur the colour image with within-channel blurring, one needs to deal with three separate problems – one for each colour channel (red, green, blue). Resulting image is then a compound of these three solutions, see Section 1.1.2.

Colour image deblurring is hence time and memory-wise considerably more expensive than the gray-scale one, which should be taken into account before opting for a specific method.

Problem 6

The last experiment compares the results obtained by the iterative methods, CGLS and LSQR, used for deblurring of a colour image. The testing image of the size 197 × 295 pixels was corrupted by the Gaussian blur with $\sigma_x = \sigma_y = 4$, and the addition of random noise with $\delta_{noise} = 10^{-1}$, see Figure 3.10.

Figure 3.10 *Testing blurred image (Left) and its exact counterpart (Right).*

To compare the two methods, we have constructed solutions corresponding to 100, 500, 1000 and 2000 iterations. Figure 3.11 shows that for $k = 100$, both solutions are equally underregularized. However, the bigger the value of the regularization parameter, the larger the difference between amounts of the inverted noise in CGLS (Left) and LSQR (Right) solutions. We see that the perturbation error in CGLS grows noticeably faster than in the LSQR solutions. After 2000 iterations, the useful information in the former solution is substantially suppressed, while the latter can still be considered quite legible.

Hence, in this case, LSQR has exhibited better regularization properties than CGLS. Nevertheless, it has been showed that in general, LSQR does not provide significantly better results than CGLS, [12].

Figure 3.11 *CGLS (Left) and LSQR (Right) solutions for different values of the regularization parameter. From top to bottom:* $k = 100, 500, 1000, 2000$*.*

Conclusion

The aim of this thesis was to provide a concise overview of the numerical techniques in digital image processing, more specifically to discuss the process of image deblurring.

Building on the explanation of digital image representation and construction of the blurring operator A, we have outlined the basic structure of the linear deblurring problem and discussed its properties. The singular value decomposition of A revealed the ill-posedness of the problem and clarified the reasons behind the failure of the direct solution methods, e.g. the Gaussian elimination. We have seen that in order to avoid the occurance of the noise-dominated solution, the discrete Picard condition needs to be satisfied and the amplification of the high frequency information must be prevented.

Hence one option is to approach the problem by means of regularization. In our discussion, we have summarized basic characteristics of the selected direct (TSVD, Tikhonov regularization) as well as iterative regularization methods (CGLS, LSQR) along with the pertinent stopping criteria – L-curve, GCV and the discrepancy principle.

The numerical experiments were carried out so as to put the theoretical background into practice. Working with the real-life image data, we have examined the role the boundary conditions and the noise level play in the image deblurring problems. Also, the colour image deblurring task was exemplified. Apart from that, we have shown that the feasibility of a specific deblurring method is difficult to estimate a priori. When using the stopping criteria for choosing the regularization parameter, one should keep in mind that the regularization and parameter-choice methods are interdependent, and the success of the solver depends on the particular input image data.

Nevertheless, regularization methods represent a powerful numerical tool for solving the image deblurring ill-posed problems and enjoy a widespread use in a raft of scientific areas.

Bibliography

[1] A. Ben-Israel and T. N. E. Greville, *Generalized Inverses: Theory and Applications*, Second edition, Springer-Verlag, New York, 2003.

[2] M. Bertaia , S. Morigi, E. Loli Piccolomini, F. Sgallari and F. Zama, *Regularization of Large Discrete Ill-Posed Problems in Image Processing*, in Donato Trigiante (Ed.), Recent Trends in Numerical Analysis, Nova Science Publishers, New York, 2000, pp. 43–57.

[3] M. Bertero and P. Boccacci, *Introduction to Inverse Problems in Imaging*, IOP Publishing Ltd, Bristol, 1998.

[4] A. Björck, *Numerical Methods for Least Squares Problems*, SIAM, Philadelphia, 1996.

[5] F. Colonna and G. R. Easley, *Generalized Discrete Radon Transforms and Applications to Image Processing*, Advances in Imaging and Electron Physics, 151 (2008), pp. 169–239.

[6] R. W. Freund, G. H. Golub and N. Nachtingal, *Iterative Solution of Linear Systems*, Acta Numerica, 1 (1991), pp. 57–100.

[7] G. H. Golub, M. Heath and G. Wahba, *Generalized Cross-Validation as a Method for Choosing a Good Ridge Parameter*, Technometrics, 21/2 (1979), pp. 215–223.

[8] G. H. Golub and C. F. Van Loan, *Matrix Computations*, Third Edition, The Johns Hopkins University Press, Baltimore, 1996.

[9] G. H. Golub, A. Hoffman and G. W. Stewart, *A Generalization of the Eckart-Young-Mirsky Matrix Approximation Theorem*, Linear Algebra and its Applications, 88-89 (1987), pp. 317–327.

[10] R. C. Gonzalez and R. E. Woods, *Digital Image Processing*, Third Edition, Pearson Prentice Hall, 2008.

[11] P. C. Hansen, *Analysis of Discrete Ill-Posed Problems by Means of the L-curve*, SIAM review, 34 (1992), pp. 561–580.

[12] P. C. Hansen, *Rank-Deficient and Discrete Ill-Posed Problems - Numerical Aspects of Linear Inversion*, SIAM, Philadelphia, 1998.

[13] P. C. Hansen, *Regularization Tools, a Matlab Package for Analysis of Discrete Regularization Problems*, Numerical Algorithms, 6 (1994), pp. 1–35.

[14] P. C. Hansen, J. G. Nagy and D. P. O'Leary, *Deblurring Images – Matrices, Spectra and Filtering*, SIAM, Philadelphia, 2006, (preprint).

[15] P. C. Hansen and D. P. O'Leary, *The Use of the L-curve in the Regularization of Discreet Ill-Posed Problems*, SIAM J. Sci. Comput., 14 (1993), pp. 1487–1503.

[16] M. R. Hestenes and E. Stiefel, *Methods of Conjugate Gradients for Solving Linear Systems*, J. Res. Nat. Bur. Stand., 49/6 (1952), pp. 409–435.

[17] I. Hnětynková , M. Plešinger and Z. Strakoš, *The Regularizing Effect of the Golub-Kahan Iterative Bidiagonalization and Revealing the Noise Level in the Data*, BIT Numerical Mathematics, 49/4 (2009), pp. 669–696.

[18] M. E. Kilmer and D. P. O'Leary, *Choosing Regularization Parameters in Iterative Methods for Ill-Posed Problems*, SIAM J. Matrix Anal. Appl., 22/4 (2001), pp. 1204–1221.

[19] A. Kirsch, *An Introduction to the Mathematical Theory of Inverse Problems*, Springer-Verlag, New York, 1996.

[20] A. J. Laub, *Matrix Analysis for Scientists and Engineers*, SIAM, Philadelphia, 2005.

[21] C. C. Paige, *Bidiagonalization of Matrices and Solution of Linear Equations*, SIAM J. Numer. Anal., 11 (1974), pp. 197–209.

[22] C. C. Paige and M. A. Saunders, *Algorithm 583. LSQR: Sparse Linear Equations and Least Squares Problems*, ACM Trans. Math. Software, 8 (1982), pp. 195–209.

[23] C. C. Paige and M. A. Saunders, *LSQR: An Algorithm for Sparse Linear Equations and Sparse Least Squares*, ACM Trans. Math. Software, 8 (1982), pp. 43–71.

[24] *PIA13196: Opportunity Amid Mars Craters*, Online image, Photojournal: NASA's Image Access Home Page, NASA/JPL-Caltech/Malin Space Science Systems, Web. 10 July 2010. <http://photojournal.jpl.nasa.gov/catalog/PIA13196>

[25] M. Razaz and R. A. Lee, *Comparison of Iterative Deconvolution and Wiener Filtering for Image Restoration*, in J. M. Blackledge (Ed.), Image Processing: Mathematical Methods and Applications, Clarendon Press, Oxford, 1997, pp. 45-159.

[26] J.-B. Sibarita, *Deconvolution Microscopy*, Adv. Biochem. Engin./Biotechnol., 95 (2005), pp. 201–243.

[27] J.J. Staal, M.D. Abramoff, M. Niemeijer, M.A. Viergever and B. van Ginneken, *Ridge Based Vessel Segmentation in Color Images of the Retina*, IEEE Transactions on Medical Imaging, 23 (2004), pp. 501–509.

[28] G. Wahba and Y. Wang, *Behaviour Near Zero of the Distribution of GCV Smoothing Parameter Estimates* Statis. Probab. Lett., 25 (1995), pp. 105-111.